ATLAS CONF Note

ATLAS-CONF-2023-060

5th September 2023

Jet radius dependence of dijet momentum balance in Pb+Pb collisions at 5.02 TeV with the ATLAS detector

The ATLAS Collaboration

This note describes a measurement of the jet radius dependence of the momentum balance between leading back-to-back dijets in 1.7 nb^{-1} of Pb+Pb collisions collected in 2018 and 260 pb^{-1} of pp collisions collected in 2017 by the ATLAS detector at the LHC. Both data sets were collected at $\sqrt{s_{\mathrm{NN}}}$ =5.02 TeV. The jets used in this analysis are reconstructed with the anti-k_t algorithm with jet radius parameters, R, of 0.2, 0.3, 0.5 and 0.6 and the momentum balance distributions are constructed for leading jets with transverse momentum (p_{T}) from 100 GeV (200 GeV) to 562 GeV for $R = 0.2$ and $R = 0.3$ ($R = 0.5$ and $R = 0.6$) jets. The results are compared to previous measurements of the same quantity made with $R = 0.4$ jets. The absolutely normalized momentum balance distributions are constructed to compare measurements in Pb+Pb collisions directly to those in pp collisions. For all jet radii considered here, there is a stronger suppression of balanced jets in central Pb+Pb collisions compared to that for imbalanced ones. For balanced jets there is no significant jet radius dependence on this suppression. For imbalanced jets, particularly at the lower selections on leading jet p_{T}, the level of suppression decreases with increasing jet radius. Additionally, pair nuclear modification factors are measured. As was previously observed for $R = 0.4$ jets, the subleading jets are found to be more suppressed than leading jets, independent of jet radius. These new measurements should provide new constraints on jet quenching scenarios in the quark-gluon plasma.

ATLAS-CONF-2023-060
19 September 2023

1 Introduction

The main physics aim of the heavy-ion program at the Large Hadron Collider (LHC) is to produce and measure the properties of the quark–gluon plasma (QGP). In quantum chromodynamics (QCD), the QGP is a high-temperature state of matter in which quarks and gluons are no longer confined in color-neutral hadrons (for a recent review, see Ref. [1]). In order to understand the properties of the QGP at short distances, high transverse momentum (p_{T})[1] probes such as jets are used [2]. Jets traversing the QGP experience *jet quenching*, characterized by a reduction in the overall jet energy compared to expectations from pp collisions. This phenomenon is understood to arise from radiative and collisional energy loss in reducing the jet p_{T} by moving energy associated with the initial parton to wider angles, with some of it ending up outside the jet cone [3]. Jet quenching is typically quantified by the overall rate of jets in a given centrality[2] interval in Pb+Pb collisions and at a given p_{T} compared to expectations from pp collisions, commonly known as the *nuclear modification factor*,

$$R_{\mathrm{AA}} = \frac{1}{N_{\mathrm{evt}}} \frac{\mathrm{d}N_{\mathrm{jet}}}{\mathrm{d}p_{\mathrm{T}}} \Bigg/ \left(\langle T_{\mathrm{AA}} \rangle \frac{\mathrm{d}\sigma_{pp}}{\mathrm{d}p_{\mathrm{T}}} \right), \tag{1}$$

where N_{jet} and σ_{pp} are the jet yield in Pb+Pb collisions and the jet cross-section in pp collisions, respectively, measured as a function of the jet p_{T}, and where N_{evt} is the total number of minimum bias Pb+Pb events and $\langle T_{\mathrm{AA}} \rangle$ is the mean nuclear thickness function [4] for the centrality interval. In the most central Pb+Pb collisions, R_{AA} is observed to be approximately 0.5, up to a p_{T} of approximately 1 TeV [5–8]. Measurements of the suppression of jets of different radii are of great interest to understand where the lost energy is with respect to the jet axis and to measure the possible response of the QGP to the presence of the jet [9]. For $p_{\mathrm{T}} > 400$ GeV in central collisions, CMS has measured no significant dependence of the jet R_{AA} on the jet radius [10]. At much lower momentum ($p_{\mathrm{T}} < 100$ GeV), measurements from ATLAS [11] found a decrease in jet quenching (an increased R_{AA}) with increasing jet radius. In contrast, recent measurements from ALICE [12] in a similar momentum region suggest that jet quenching increases for larger radii jets at fixed p_{T}. The shape modification of jets in dijets has been less studied; however, CMS found modifications in the jet shape for subleading jets in imbalanced dijets for leading jets with $p_{\mathrm{T}} > 120$ GeV [13]. For recent reviews of jet quenching, see Refs. [2, 14].

Jets are largely produced in pairs in $2 \rightarrow 2$ partonic scattering processes. The QCD evolution of the partons after the scattering gives rise to back-to-back jets, referred to here as "dijets". In heavy-ion collisions, dijets provide a complementary probe to single jets for studying jet quenching. The two jets are expected to experience asymmetric energy loss due to traversing unequal path lengths in the QGP [15], driven by the geometry of the overlapping nuclei and the relative orientation of the jet trajectories through the QGP. Measurements of the azimuthal anisotropy of jets [16] have shown that the geometry of the overlapping nuclei affects the relative rates of jets measured in Pb+Pb collisions. Additionally, jets are also expected to experience jet-by-jet fluctuations in the energy-loss process [17]. In general, the measurement of the

[1] ATLAS uses a right-handed coordinate system with its origin at the nominal interaction point (IP) in the center of the detector, and the z-axis along the beam pipe. The x-axis points from the IP to the center of the LHC ring, and the y-axis points upward. Cylindrical coordinates (r, ϕ) are used in the transverse plane, ϕ being the azimuthal angle around the z-axis. The pseudorapidity is defined in terms of the polar angle θ as $\eta = -\ln\tan(\theta/2)$. The rapidity is defined as $y = 0.5 \ln[(E + p_z)/(E - p_z)]$ where E and p_z are the energy and z-component of the momentum along the beam direction, respectively. Transverse momentum and transverse energy are defined as $p_{\mathrm{T}} = p \sin\theta$ and $E_{\mathrm{T}} = E \sin\theta$, respectively. The angular distance between two objects with relative differences $\Delta\eta$ in pseudorapidity and $\Delta\phi$ in azimuth is given by $\Delta R = \sqrt{(\Delta\eta)^2 + (\Delta\phi)^2}$.

[2] Centrality characterizes the degree to which the colliding nuclei overlap. The most central collisions have large overlap and the highest particle multiplicities, while the most peripheral collisions have only minimal overlap and have particle multiplicities closer to those of pp collisions at the same nucleon–nucleon collision energy.

p_{T} balance of dijets provides a way to constrain the relative importance of fluctuations and geometry in jet quenching. Measurements of the jet radius dependence of the dijet balance are especially interesting and can provide different sensitivity to the location of the lost energy than is available with single jet measurements.

In order to compare the transverse momenta of the two jets which comprise a dijet, the leading dijet momentum balance:

$$x_{\mathrm{J}} \equiv p_{\mathrm{T},2}/p_{\mathrm{T},1} \tag{2}$$

is measured. The leading dijet is constructed using the two highest p_{T} jets out of the set of jets in an event, $p_{\mathrm{T},1}$ is the transverse momentum of the highest-p_{T} (leading) jet, and $p_{\mathrm{T},2}$ is the transverse momentum of the second-highest-p_{T} (subleading) jet.

In pp collisions, the showering process in vacuum, as well as higher-order scattering processes, can lead to imbalanced dijet transverse momenta. However, the most probable situation is that the jets are nearly balanced in p_{T} [18, 19]. Previous dijet measurements in Pb+Pb collisions have shown that jets are more likely to be more imbalanced in Pb+Pb collisions than in pp collisions [18–21].

Early dijet publications reported only the imbalance normalized by the measured dijet yields [18, 20, 21], in order to study the changes in the shape of the x_{J} distribution as a function of the heavy-ion collision centrality. Ref. [19] addressed the absolute rate at which dijets are produced in Pb+Pb collisions, which could assess whether leading dijets are suppressed at levels similar to those for inclusive jets [5]. This note extends the studies in Ref. [19] by varying the jet radius parameter with leading dijets in Pb+Pb and pp collisions at $\sqrt{s_{\mathrm{NN}}} = 5.02$ TeV. These measurements use 1.7 nb^{-1} of Pb+Pb collisions collected in 2018 as well as 260 pb^{-1} of pp data collected in 2017 with the ATLAS detector [22] at the LHC.

Jets are reconstructed using the anti-k_t algorithm [23] with radius parameters $R = 0.2$, $R = 0.3$, $R = 0.5$, and $R = 0.6$. Results from this paper are directly compared to the $R = 0.4$ results from Ref. [19] which use the same analysis method and binning. The analysis is conducted independently for each of the radius values. In each case, leading dijets are constructed from the two highest-p_{T} jets in the event and are required to have the two jets nearly back-to-back in azimuth with $\Delta\phi \equiv |\phi_1 - \phi_2| \geq 7\pi/8$ and $|y| < 2.1$. The measurement is performed for p_{T} values from 100 (200) to 562 GeV for $R = 0.2$ and $R = 0.3$ ($R = 0.5$ and $R = 0.6$) for leading jets. Following Ref. [19], subleading jets are reported down to x_{J} values of 0.32 for each leading jet p_{T} selection. Most dijets have x_{J} greater than 0.32, making this analysis not very sensitive to the exact value of this requirement. Events in which the two highest-p_{T} jets do not meet the selection criteria are discarded.

The primary observable for this measurement is the two-dimensional yield of leading dijets (N_{pair}) meeting the selection criteria:

$$\frac{\mathrm{d}^2 N_{\mathrm{pair}}}{\mathrm{d}p_{\mathrm{T},1}\mathrm{d}p_{\mathrm{T},2}}. \tag{3}$$

Projections of these two-dimensional distributions can be used to construct x_{J} distributions as a function of $p_{\mathrm{T},1}$ and $p_{\mathrm{T},2}$. The x_{J} values, as defined in Eq. (2), are reported for $0.32 < x_{\mathrm{J}} < 1.0$ for selections in $p_{\mathrm{T},1}$. This note presents results of the *absolutely normalized* x_{J} distributions:

$$\frac{1}{L_{pp}}\frac{\mathrm{d}N^{pp}_{\mathrm{pair}}}{\mathrm{d}x_{\mathrm{J}}} \tag{4}$$

in pp collisions and

$$\frac{1}{\langle T_{\mathrm{AA}}\rangle N_{\mathrm{evt}}^{\mathrm{AA}}}\frac{\mathrm{d}N_{\mathrm{pair}}^{\mathrm{AA}}}{\mathrm{d}x_{\mathrm{J}}} \tag{5}$$

in Pb+Pb collisions. Here $\langle T_{\mathrm{AA}}\rangle$ and $N_{\mathrm{evt}}^{\mathrm{AA}}$ are defined the same way as in Eq. (1) and L_{pp} is the integrated luminosity of the pp collisions [24].

The absolutely normalized x_{J} distributions allow a direct comparison between the dijet rates measured in Pb+Pb and pp collisions. This comparison is quantified by the ratio J_{AA}:

$$J_{\mathrm{AA}} \equiv \frac{1}{\langle T_{\mathrm{AA}}\rangle N_{\mathrm{evt}}^{\mathrm{AA}}}\frac{\mathrm{d}N_{\mathrm{pair}}^{\mathrm{AA}}}{\mathrm{d}x_{\mathrm{J}}} \Bigg/ \left(\frac{1}{L_{pp}}\frac{\mathrm{d}N_{\mathrm{pair}}^{pp}}{\mathrm{d}x_{\mathrm{J}}}\right). \tag{6}$$

Finally, the absolutely normalized x_{J} distributions can be integrated over the measurement range of $0.32 < x_{\mathrm{J}} < 1.0$ (and the corresponding ranges in $p_{\mathrm{T},1}$ and $p_{\mathrm{T},2}$) to construct the pair nuclear modification factors for dijets as a function of the leading and subleading jet p_{T}. These quantities were first shown in Ref. [19] and are defined analogously to the nuclear modification factor for inclusive jets, Eq. (1), as:

$$R_{\mathrm{AA}}^{\mathrm{pair}}(p_{\mathrm{T},1}) = \frac{\frac{1}{\langle T_{\mathrm{AA}}\rangle N_{\mathrm{evt}}^{\mathrm{AA}}}\int_{0.32\times p_{\mathrm{T},1}}^{p_{\mathrm{T},1}}\frac{\mathrm{d}^2N_{\mathrm{pair}}^{\mathrm{AA}}}{\mathrm{d}p_{\mathrm{T},1}\mathrm{d}p_{\mathrm{T},2}}\mathrm{d}p_{\mathrm{T},2}}{\frac{1}{L_{pp}}\int_{0.32\times p_{\mathrm{T},1}}^{p_{\mathrm{T},1}}\frac{\mathrm{d}^2N_{\mathrm{pair}}^{pp}}{\mathrm{d}p_{\mathrm{T},1}\mathrm{d}p_{\mathrm{T},2}}\mathrm{d}p_{\mathrm{T},2}} \tag{7}$$

and

$$R_{\mathrm{AA}}^{\mathrm{pair}}(p_{\mathrm{T},2}) = \frac{\frac{1}{\langle T_{\mathrm{AA}}\rangle N_{\mathrm{evt}}^{\mathrm{AA}}}\int_{p_{\mathrm{T},2}}^{p_{\mathrm{T},2}/0.32}\frac{\mathrm{d}^2N_{\mathrm{pair}}^{\mathrm{AA}}}{\mathrm{d}p_{\mathrm{T},1}\mathrm{d}p_{\mathrm{T},2}}\mathrm{d}p_{\mathrm{T},1}}{\frac{1}{L_{pp}}\int_{p_{\mathrm{T},2}}^{p_{\mathrm{T},2}/0.32}\frac{\mathrm{d}^2N_{\mathrm{pair}}^{pp}}{\mathrm{d}p_{\mathrm{T},1}\mathrm{d}p_{\mathrm{T},2}}\mathrm{d}p_{\mathrm{T},1}}. \tag{8}$$

By integrating over $p_{\mathrm{T},2}$ ($p_{\mathrm{T},1}$), one can access information from $R_{\mathrm{AA}}^{\mathrm{pair}}(p_{\mathrm{T},1})$ ($R_{\mathrm{AA}}^{\mathrm{pair}}(p_{\mathrm{T},2})$) about the differential rate of dijet production in leading (subleading) jet p_{T} bins. Comparison of these two quantities at a fixed jet p_{T} provides information about the suppression of leading and subleading jets.

2 ATLAS detector

The ATLAS detector [22] at the LHC is a multipurpose particle detector with a forward–backward symmetric cylindrical geometry and a near-4π coverage in solid angle. It consists of an inner tracking detector surrounded by a thin superconducting solenoid, electromagnetic and hadron calorimeters, and a muon spectrometer. The inner-detector system is immersed in a 2 T axial magnetic field and provides charged-particle tracking within $|\eta| < 2.5$. The high-granularity silicon pixel detector covers the vertex region and typically provides four measurements per track, with the first hit typically being in the insertable B-layer installed before Run 2 [25, 26]. It is followed by the silicon microstrip tracker (SCT) which usually provides eight measurements per track. These silicon detectors are complemented by the transition radiation tracker, a drift-tube-based detector, which surrounds the SCT and has coverage up to $|\eta| = 2.0$.

The calorimeter system covers the pseudorapidity range $|\eta| < 4.9$. Within the region $|\eta| < 3.2$, electromagnetic calorimetry is provided by barrel and endcap high-granularity lead/liquid-argon (LAr) calorimeters, with an additional thin LAr presampler covering $|\eta| < 1.8$ to correct for energy loss in material

upstream of the calorimeters. Hadronic calorimetry is provided by the steel/scintillator-tile calorimeter, segmented into three barrel structures within $|\eta| < 1.7$, and two copper/LAr hadronic endcap calorimeters. The solid angle coverage is completed with copper/LAr and tungsten/LAr calorimeter modules (FCal), covering the forward regions of $3.1 < |\eta| < 4.9$. The zero-degree calorimeters (ZDC) consist of layers of alternating quartz rods and tungsten plates and are located symmetrically at $z = \pm 140$ m and cover $|\eta| \geq 8.3$. In Pb+Pb collisions, the ZDCs primarily measure 'spectator' neutrons: neutrons that do not interact hadronically when the incident nuclei collide.

Events of interest are selected for recording and offline analysis by the first-level (L1) trigger system implemented in custom hardware, followed by selections made by algorithms implemented in software in the high-level trigger [27].

An extensive software suite [28] is used in data simulation, in reconstruction and analysis of real and simulated events, in detector operations, and in the trigger and data acquisition systems of the experiment. The events used in this analysis were selected by a jet trigger [27]. The L1 trigger identified jet candidates by applying a sliding-window algorithm and selecting events passing a E_{T} threshold of 30 GeV. These events were then passed to the high-level jet trigger, which uses a jet reconstruction and background subtraction procedure similar to that used in the offline analysis and requires a minimum $p_{\mathrm{T}}^{\mathrm{jet}}$ of 100 GeV for anti-k_t $R = 0.4$ jets. The jet trigger efficiencies were evaluated separately for each of the jet radii considered here. The thresholds were set such that the triggers were fully efficient for each R value over the $p_{\mathrm{T}}^{\mathrm{jet}}$ range considered in this measurement.

3 Data and Monte Carlo selection

The Pb+Pb data used to perform these measurements were collected in 2018, and the pp data used were collected in 2017 with the average number of inelastic interactions per bunch crossing ranging from 1.4 to 4.4. Events were selected by minimum-bias and jet triggers [29]. Although only a small fraction of the Pb+Pb events ($< 0.5\%$) contain multiple collisions, these were suppressed utilizing the observed anti-correlation, expected from the nuclear geometry, between the total transverse energy deposited in both of the forward calorimeters, $\Sigma E_{\mathrm{T}}^{\mathrm{FCal}}$, and the energy in both ZDCs, which is proportional to the number of observed spectator neutrons. Pileup collisions are not rejected in pp collisions.

The overlap area of the two colliding nuclei in Pb+Pb collisions is characterized by the event centrality, which is estimated from the total transverse energy deposited in the FCal [30]. This measurement considers five centrality intervals as defined according to successive percentiles of the $\Sigma E_{\mathrm{T}}^{\mathrm{FCal}}$ distribution obtained from minimum-bias collisions. The centrality intervals considered in this measurement are 0–10% (largest $\Sigma E_{\mathrm{T}}^{\mathrm{FCal}}$), 10–20%, 20–40%, 40–60%, and 60–80% (smallest $\Sigma E_{\mathrm{T}}^{\mathrm{FCal}}$). The values of the mean nuclear thickness function, $\langle T_{\mathrm{AA}} \rangle$ [4], are determined using the TGlauberMC v3.2 package [31]; the uncertainties in $\langle T_{\mathrm{AA}} \rangle$ are discussed in Ref. [32]. The $\langle T_{\mathrm{AA}} \rangle$ values and their uncertainties are listed in Table 1 for each centrality selection considered in this measurement.

This analysis uses four Monte Carlo (MC) samples to evaluate the detector performance and correct for detector effects. The pp MC sample used in this analysis includes 3.2×10^7 Pythia 8 [33] pp jet events generated at $\sqrt{s} = 5.02$ TeV with parameter values set according to the A14 tune [34] and the NNPDF23lo parton distribution functions (PDFs) [35]. Pileup due to additional inelastic pp interactions is similarly generated using Pythia 8 with the same PDFs and utilizing the A3 tune [36], tuned for inclusive QCD processes, matching the number of extra collisions in the pp data. The MC sample for Pb+Pb collisions

Table 1: The $\langle T_{\mathrm{AA}} \rangle$ values and uncertainties for the centrality selections used in this measurement. These are the results from TGlauberMC v3.2 modeling of the summed transverse energy in the forward calorimeters, $\Sigma E_{\mathrm{T}}^{\mathrm{FCal}}$.

Centrality selection	$\langle T_{\mathrm{AA}} \rangle \pm \delta\langle T_{\mathrm{AA}} \rangle$ [1/mb]
0–10%	23.35 ± 0.20
10–20%	14.33 ± 0.17
20–40%	6.79 ± 0.16
40–60%	1.96 ± 0.09
60–80%	0.39 ± 0.03

used the 2018 detector conditions and contains 3.2×10^7 pp Pythia 8 events with the same A14 tune and PDFs as used for the generation of the pp jet MC samples. The underlying event contribution to the detector signal is accounted for by overlaying the simulated pp events with dedicated Pb+Pb data events from the Pb+Pb run. The data events from Pb+Pb collisions were combined with the signal from the Pythia 8 simulation of hard scattering events at the digitization stage, and then reconstructed as a combined event. This procedure enables the "data overlay" sample to accurately reproduce the effects of the underlying event on the jet response. This sample was reweighted on an event-by-event basis to ensure the same centrality distribution as is measured in the jet-triggered data samples. The detector response in all three MC samples was simulated utilizing Geant4 [37, 38]. Finally, pp Herwig++ [39] events using the UEEE5 tune [40] and the CTEQ6L1 PDFs [41] are used for uncertainty studies.

4 Jet reconstruction and performance

The jet reconstruction procedures follow those used by ATLAS for previous jet measurements in Pb+Pb collisions [5, 16]. Jets are reconstructed using the anti-k_t algorithm [23] implemented in the FastJet software package [42]. In both pp and Pb+Pb collisions, jets with $R = 0.2$, $R = 0.3$, $R = 0.5$, and $R = 0.6$ are formed by clustering calorimetric towers of spatial size $\Delta\eta \times \Delta\phi = 0.1 \times \pi/32$. In Pb+Pb collisions, a background subtraction procedure is applied to estimate, within each event, the underlying event (UE) average transverse energy density, $\rho(\eta, \phi)$, where the ϕ dependence is due to global azimuthal correlations in the particle production from the hydrodynamic flow [43]. The modulation accounts for the contribution to the UE of the second-, third-, and fourth-order azimuthal anisotropy harmonics characterized by values of flow coefficients v_n^{UE} [43]. An iterative procedure is used to remove the impact of jets on the estimated ρ and v_n^{UE} values. Jet R-, η-, and p_{T}-dependent correction factors derived in simulations are applied to the measured jet energy to correct for the calorimeter energy response [44, 45]. An additional correction based on in situ studies of jets recoiling against photons and jets in other regions of the calorimeter is applied to account for differences between the data and MC [46]. This calibration is followed by a "cross-calibration" that relates the jet energy scale (JES) of jets reconstructed by the procedure outlined in this section to the JES in 13 TeV pp collisions, which allows for the use of uncertainties obtained for the latter [45].

"Truth"-level jets are defined in the MC sample before detector simulation by applying the anti-k_t algorithm with $R = 0.2$, $R = 0.3$, $R = 0.5$, and $R = 0.6$ to stable particles with a proper lifetime greater than 30 ps, but excluding muons and neutrinos, which do not leave significant energy deposits in the calorimeter. After the detector simulation the truth jets are matched to the nearest reconstructed jet within $\Delta R < 0.75R$. The performance of the jet reconstruction is characterized by the JES and jet energy resolution (JER), which correspond to the mean and variance, respectively, of the $p_{\mathrm{T}}^{\mathrm{reco}}/p_{\mathrm{T}}^{\mathrm{truth}}$ distribution, where $p_{\mathrm{T}}^{\mathrm{reco}}$ is

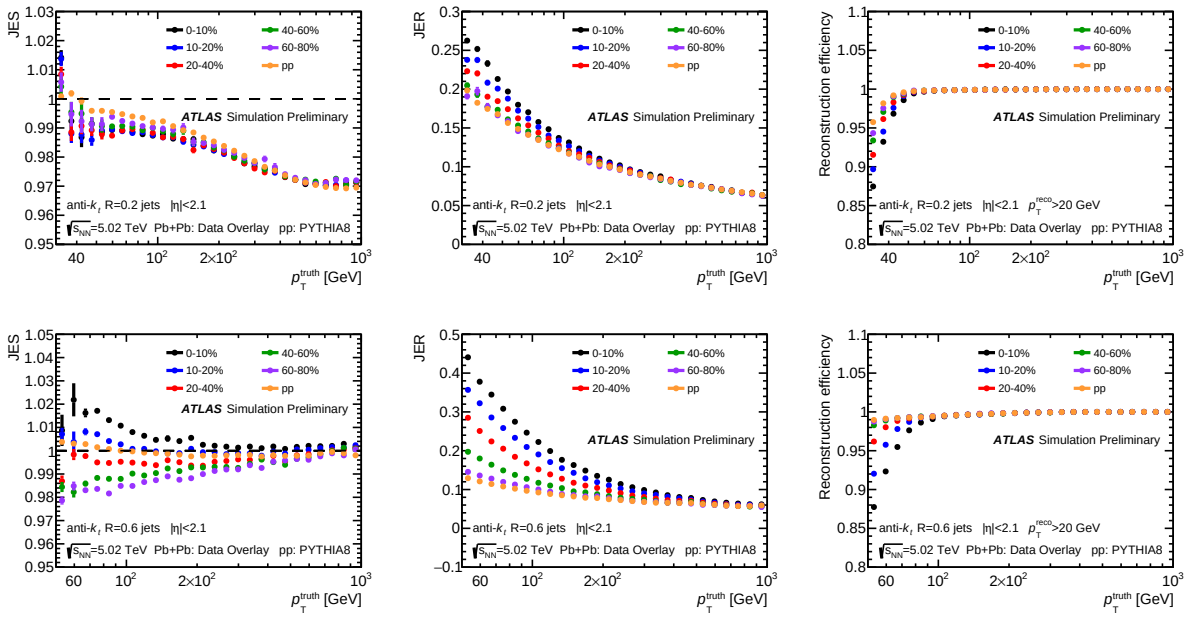

Figure 1: The JES (left), JER (middle), and jet reconstruction efficiency (right) for $R = 0.2$ (top) and $R = 0.6$ (bottom) jets in pp collisions and the centrality selections in Pb+Pb collisions used in this analysis.

the reconstructed jet p_{T} and $p_{\mathrm{T}}^{\mathrm{truth}}$ is the p_{T} of the matched truth-level jet. The JES and JER as a function of $p_{\mathrm{T}}^{\mathrm{truth}}$ can be seen in Fig. 1 for $R = 0.2$ and $R = 0.6$ jets. The decrease in the JES for $R = 0.2$ jets with $p_{\mathrm{T}}^{\mathrm{truth}} \lesssim 50$ GeV in Pb+Pb collisions stems from jets for which there is an over-subtraction of the underlying event. The deviation of JES from unity for high-p_{T} $R = 0.2$ jets is due to the different cuts used in the determination of the jet calibration compared to this analysis. Both of these effects are corrected for by the unfolding procedure described below. The efficiency of reconstructing a jet with $p_{\mathrm{T}} > 20$ GeV, as evaluated from the probability of a truth-jet matching to a reconstructed jet, can also be seen as a function of $p_{\mathrm{T}}^{\mathrm{truth}}$ in Fig. 1.

5 Data analysis

The analysis and dijet selection used here closely follow those in Ref. [19]. In each data event, the reconstructed leading dijet is constructed from the two highest-$p_{\mathrm{T}}^{\mathrm{reco}}$ jets in the event with reconstructed leading $p_{\mathrm{T},1}^{\mathrm{reco}} > 79$ GeV for $R = 0.2$ and $R = 0.3$ jets, $p_{\mathrm{T},1}^{\mathrm{reco}} > 121$ GeV for $R = 0.5$ and $R = 0.6$ jets, and reconstructed subleading $p_{\mathrm{T},2}^{\mathrm{reco}} > 32$ GeV for $R = 0.2$ and $R = 0.3$ jets, $p_{\mathrm{T},2}^{\mathrm{reco}} > 41$ GeV for $R = 0.5$ jets, and $p_{\mathrm{T},2}^{\mathrm{reco}} > 51$ GeV for $R = 0.6$ jets. The minimum $p_{\mathrm{T},1}^{\mathrm{reco}}$ was based on the minimum p_{T} for which the trigger is fully efficient for the various jet radii. The minimum $p_{\mathrm{T},2}^{\mathrm{reco}}$ was based on 0.32 of the minimum p_{T} for which the rate of jets created by UE fluctuations becomes negligible. Both jets are required to have $|y| < 2.1$. These selections provide an underflow region for the unfolding to enable inflow and outflow of jets from the measurement region. These dijets are required to be back-to-back with $|\Delta\phi| > 7\pi/8$. Events in which the leading dijets do not meet these criteria are discarded. For dijets matching the selection criteria, two-dimensional $(p_{\mathrm{T},1}^{\mathrm{reco}}, p_{\mathrm{T},2}^{\mathrm{reco}})$ distributions are constructed symmetrically across $p_{\mathrm{T},1}^{\mathrm{reco}} = p_{\mathrm{T},2}^{\mathrm{reco}}$. The distributions are symmetrized to account for the possibility of swapping the leading and subleading jet

definition due to the finite JER.

The measured $(p_{\mathrm{T},1}^{\mathrm{reco}}, p_{\mathrm{T},2}^{\mathrm{reco}})$ distributions are a combination of the dijet signal and pairs of uncorrelated jets. Since the underlying-event subtraction accounts for azimuthal correlations in the particle production due to hydrodynamic flow, the contribution from uncorrelated dijets is largely independent of the $\Delta\phi$ of the jets; therefore, a $\Delta\phi$ sideband method is used to remove these pairs as a function of $(p_{\mathrm{T},1}^{\mathrm{reco}}, p_{\mathrm{T},2}^{\mathrm{reco}})$. The symmetrized two-dimensional $(p_{\mathrm{T},1}^{\mathrm{reco}}, p_{\mathrm{T},2}^{\mathrm{reco}})$ distribution of background combinatoric dijets is determined using dijets with $1 < |\Delta\phi| < 1.4$ which, after normalizing to the $\Delta\phi$ window of the signal band, is subtracted from the dijet yields. This effect is strongest for 0–10% centrality Pb+Pb events at low $p_{\mathrm{T},1}^{\mathrm{reco}}$. In the most central collisions, combinatoric dijets constitute 2% of the $R = 0.2$ dijets with $p_{\mathrm{T},1}^{\mathrm{reco}} > 100$ GeV and $p_{\mathrm{T},2}^{\mathrm{reco}} > 32$ GeV, and 1% of the $R = 0.6$ dijets with $p_{\mathrm{T},1}^{\mathrm{reco}} > 158$ GeV and $p_{\mathrm{T},2}^{\mathrm{reco}} > 51$ GeV. The combinatoric dijet rate drops off rapidly both with increasing $p_{\mathrm{T},1}^{\mathrm{reco}}$ and in more peripheral events. Because of how the leading dijet is defined, the presence of residual combinatoric dijets in the sample results in an inefficiency for genuine jet pairs, where one of the jets might be superseded by an uncorrelated third jet. This effect is corrected for using the measured inclusive jet spectrum from minimum-bias events to determine the efficiency loss as a function of the measured jet p_{T} following the method discussed in Ref. [18].

In order to correct for the effects of the JES and JER, the measured $(p_{\mathrm{T},1}^{\mathrm{reco}}, p_{\mathrm{T},2}^{\mathrm{reco}})$ distributions are unfolded using the iterative Bayesian unfolding procedure [47] as implemented in the RooUnfold [48] software package. A two-dimensional unfolding is used in order to account for bin migration of both the leading and the subleading jet p_{T}, as well as to account for possible swapping of the leading and subleading jet. Separate response matrices are generated for pp collisions as well as for each centrality selection in Pb+Pb collisions for each R value used in this analysis. The response matrix used in the unfolding contains the relationship between $(p_{\mathrm{T},1}^{\mathrm{truth}}, p_{\mathrm{T},2}^{\mathrm{truth}})$ and $(p_{\mathrm{T},1}^{\mathrm{reco}}, p_{\mathrm{T},2}^{\mathrm{reco}})$. It is populated by identifying the leading and subleading truth-level jets in the MC sample which are matched to the corresponding reconstructed jets within $\Delta R < 0.75R$. In order to account for migration from lower jet $p_{\mathrm{T}}^{\mathrm{reco}}$, the response matrices are populated with truth-level jets down to $p_{\mathrm{T},1}^{\mathrm{truth}}$ of 20 GeV and $p_{\mathrm{T},2}^{\mathrm{truth}}$ of 10 GeV. As with the reconstructed data, truth dijets are required to have $|\Delta\phi_{\mathrm{truth}}| > 7\pi/8$, with each jet being within $|y_{\mathrm{truth}}| < 2.1$. The two selected reconstructed jets from the MC simulations are required to meet the same selection criteria as applied to dijets measured in data. Truth dijets that do not match to a reconstructed dijet meeting the selection criteria are accounted for by using an efficiency correction in the unfolding. Similarly to the construction of the data distributions, the response matrix is populated symmetrically in $p_{\mathrm{T},1}$ and $p_{\mathrm{T},2}$. The unfolding requires an assumption of an initial distribution, referred to here as the prior, which is similar to the measured distributions. Here, the to generate the prior, the response matrices are reweighted along the $p_{\mathrm{T},1}^{\mathrm{truth}}$ and $p_{\mathrm{T},2}^{\mathrm{truth}}$ axes by the ratio of the two-dimensional reconstructed yields in data to those from simulation. The number of iterations used in the unfolding is tuned separately for each centrality in Pb+Pb collisions and for pp collisions. The number of iterations in each case was selected to optimize the balance between the accuracy of the final unfolded yield, and the increased statistical uncertainty which results from a larger number of iterations. In Pb+Pb collisions, the number of iterations was largest for central events and larger radii; two iterations were used for $R = 0.2$ jets in 60–80% central Pb+Pb collisions, while seven iterations were used for the $R = 0.6$ jets in 0–10% central Pb+Pb collisions. In pp collisions, the number of iterations increased with the jet radii; seven iterations were used for $R = 0.6$ jets and three iterations were used for $R = 0.2$ jets.

In order to evaluate the statistical uncertainties of the data and the MC simulation, 100 unfoldings were performed by varying each bin in either the data distribution or the response matrix independently according to its statistical uncertainty while preserving the symmetrization across $p_{\mathrm{T},1} = p_{\mathrm{T},2}$. The standard deviation

of the resulting unfolded distributions in each $(p_{\mathrm{T},1}, p_{\mathrm{T},2})$ bin was taken as the contribution to the statistical uncertainty on the corresponding unfolded $(p_{\mathrm{T},1}, p_{\mathrm{T},2})$ bin. The data and response matrix statistical uncertainty components were combined in quadrature in order to obtain the total statistical uncertainty of the unfolded distributions. Due to the large number of bins in the two-dimensional unfolding, in some cases the uncertainties due to the finite MC sample sizes are comparable to those in the data.

To extract measurements of the dijet momentum balance observable, x_{J}, the unfolded two-dimensional $(p_{\mathrm{T},1}, p_{\mathrm{T},2})$ distributions are first reflected about $p_{\mathrm{T},1} = p_{\mathrm{T},2}$ in order to restore the leading/subleading hierarchy. Then, following the procedure discussed in Refs. [18, 19, 49], the two-dimensional distributions are projected in slices of $p_{\mathrm{T},1}$ into bins of x_{J}.

After projecting the resulting distributions over selections of $p_{\mathrm{T},1}$, the absolutely-normalized x_{J} distributions are extracted by instead normalizing the x_{J} distributions by either the number of events and the $\langle T_{\mathrm{AA}} \rangle$ in Pb+Pb collisions or the integrated luminosity in pp collisions, as described by Exp. (5). The self-normalized x_{J} distributions can be extracted by normalizing by the number of dijets (N_{pair}) and accounting for the x_{J} bin widths.

6 Systematic uncertainties

Systematic uncertainties for this measurement are attributed to three categories of sources, those which arise from the analysis and unfolding procedure, those which stem from uncertainties in the jet energy resolution (JER) and scale (JES), and those arising from the global normalization. For each uncertainty component in the first two categories, the entire analysis procedure is repeated accounting for the modification to the analysis procedure or the response matrix and the result is compared with the nominal one. The third category applies to the absolutely-normalized x_{J} distributions, J_{AA} distributions, $R_{\mathrm{AA}}^{\mathrm{pair}}(p_{\mathrm{T},1})$, and $R_{\mathrm{AA}}^{\mathrm{pair}}(p_{\mathrm{T},2})$; it contains the uncertainty in the determination of the mean nuclear thickness function, $\langle T_{\mathrm{AA}} \rangle$, and the pp luminosity. These uncertainties are independent of the jet transverse momentum and are noted on the figures.

The systematic uncertainty in the JES has five parts. First, a centrality-independent baseline component is determined from in situ studies of the calorimeter response to jets reconstructed with the procedure used in 13 TeV pp collisions [50]. A second, centrality-independent component accounts for the relative energy scale difference between the jet reconstruction procedures used in this analysis and those in 13 TeV pp collisions. This is evaluated using the cross-calibration procedure described in Ref. [45]. Potential inaccuracies in the Pythia 8 MC sample's description of the relative abundances of jets initiated by quarks and gluons and of the calorimetric response to quark and gluon jets are accounted for by the third, centrality-independent, component is based on evaluating these same quantities using the Herwig++ MC sample. The fourth, centrality-dependent, component accounts for modifications of the parton shower due to quenching [51], which is not modeled in the simulations. The modifications to the parton shower can impact the detector response to jets in Pb+Pb collisions resulting in a small disagreement in the JES between data and simulations. The extent of this disagreement, and corresponding uncertainty contribution is evaluated by the method used in Ref. [45] for 2015 and 2011 data, which compares the jet p_{T} measured in the calorimeter with the sum of the transverse momenta of charged particles within the jet, in both the data and MC samples. This uncertainty is determined as a function of event centrality and was found to be independent of jet p_{T} and η. The selected charged-particle tracks have $p_{\mathrm{T}} > 4$ GeV in order to exclude particles from the UE. The sum of the charged-particle transverse momenta provides a data-driven estimate

of the centrality dependence of the JES arising from the observed centrality-dependent modification of the jet fragmentation due to jet quenching in Pb+Pb collisions [51]. The size of this centrality-dependent uncertainty in the JES reaches 1.2% in the most central collisions and the value is applied independent of x_{J}. The systematic uncertainties from the JES discussed above are derived for $R = 0.4$ jets. The fifth component does not depend on collision centrality for $R = 0.2$ and $R = 0.3$ jets and contains a centrality dependent contribution for $R = 0.5$ and $R = 0.6$ jets and it accounts for the potential difference in uncertainties between $R = 0.4$ and jets with the radii used here. The centrality independent component is assessed by comparing the ratio of p_{T} for matched $R = 0.2$, $R = 0.3$, $R = 0.5$, and $R = 0.6$ jets with $R = 0.4$ jets measured in data and the MC sample. For each individual component, the JES in the MC simulation was modified as a function of p_{T} and η by one standard deviation, and the response matrix was recomputed.

The uncertainty due to the JER is evaluated by repeating the unfolding procedure with modified response matrices, where an additional contribution is added to the resolution of the reconstructed p_{T} in the MC sample using a Gaussian smearing procedure. The smearing factor is evaluated using an in situ technique in 13 TeV pp data that involves studies of dijet p_{T} balance [52]. Further, an uncertainty is included to account for differences between the tower-based jet reconstruction and the jet reconstruction used in analyses of 13 TeV pp data, as well as differences in calibration procedures. Similarly to the JES, an additional uncertainty is assigned to the JER to account for differences between the jets used in this analysis and $R = 0.4$ jets. The modifications to the response are propagated through the unfolding and the resulting uncertainty is symmetrized.

Two sources of systematic uncertainty were included to account for uncertainties in the removal of the combinatoric background. The first contribution stems from the combinatoric subtraction method, and was determined by extracting the two-dimensional $(p_{\mathrm{T},1}, p_{\mathrm{T},2})$ distribution of combinatoric jets from an alternative sideband of $1.1 < |\Delta\phi| < 1.5$ as was done in Refs. [18, 19]. The second contribution stems from the sensitivity of the analysis to the efficiency correction for combinatoric jets, and was evaluated by repeating the analysis without the inclusion of this efficiency correction. The deviation from the nominal result is taken as the uncertainty contribution.

Additional sources of systematic uncertainty which account for the unfolding procedure were considered. The sensitivity to the Bayesian prior was evaluated by modifying the weights applied when producing the response matrix in a centrality-dependent manner in order to enclose the data $(p_{\mathrm{T},1}^{\mathrm{reco}}, p_{\mathrm{T},2}^{\mathrm{reco}})$ distributions between the corresponding MC distributions based on the nominal and alternative priors. There is a sensitivity to the minimum $p_{\mathrm{T}}^{\mathrm{jet}}$ in the analysis at small x_{J} and small $p_{\mathrm{T},1}$ due to the efficiency correction made as part of the unfolding. The sensitivity of the result to this effect is evaluated by varying the minimum reconstructed $p_{\mathrm{T}}^{\mathrm{jet}}$, motivated by the magnitude of the JER, from 32 to 39 GeV for $R = 0.2$ and $R = 0.3$ jets, from 41 to 51 GeV for $R = 0.5$ jets, from 51 to 63 GeV for $R = 0.6$ jets, for both data and simulation. This results in a significant contribution to the systematic uncertainties at low x_{J} in low $p_{\mathrm{T},1}$ bins. For each of these contributions the deviation of the unfolded result from the nominal is symmetrized and taken as a contribution to the systematic uncertainties. Additionally, a closure test was performed using the MC samples by splitting them into two equal parts and using one part to produce a response matrix and the other in place of the data sample in the unfolding. The deviation between the unfolded result and the underlying truth-level distribution was taken as an estimate of this uncertainty. The uncertainty from each of these contributions is taken independently and symmetrized.

The magnitude of the systematic uncertainties in the absolutely-normalized x_{J} distributions can be seen in Fig. 2 for both central Pb+Pb and pp collisions and $R = 0.2$ and $R = 0.6$ jets. In the central collisions for $R = 0.2$ jets, the total systematic uncertainties are driven by the JES and JER systematic uncertainties; for $R = 0.6$ jets in these collisions, the total systematic uncertainties are largely driven by the sensitivity of the

unfolding to the choice of prior. In contrast, in pp collisions, the total uncertainties are largely driven by the uncertainty in the JES and JER for all radii. The fractional uncertainties are largest at low x_{J} in both collision systems; however, the yield in these x_{J} regions is small.

The systematic uncertainty contributions are similarly propagated to the calculation of the nuclear modification factor. The centrality-independent components of the JES and JER, and the centrality independent part of the jet radius dependent uncertainty are treated as correlated between Pb+Pb and pp collisions. The remainder of the contributions to the systematic uncertainty are treated as uncorrelated between Pb+Pb and pp. The resulting uncertainties in $R_{\mathrm{AA}}^{\mathrm{pair}}(p_{\mathrm{T},1})$ and $R_{\mathrm{AA}}^{\mathrm{pair}}(p_{\mathrm{T},2})$ are shown for 0–10% centrality Pb+Pb collisions in Fig. 3; these uncertainties are dominated by the JES uncertainty. In the ratio of $R_{\mathrm{AA}}^{\mathrm{pair}}(p_{\mathrm{T},2})$ to $R_{\mathrm{AA}}^{\mathrm{pair}}(p_{\mathrm{T},1})$, each source of systematic uncertainty is treated as fully correlated between $R_{\mathrm{AA}}^{\mathrm{pair}}(p_{\mathrm{T},2})$ and $R_{\mathrm{AA}}^{\mathrm{pair}}(p_{\mathrm{T},1})$, including the global systematic uncertainties.

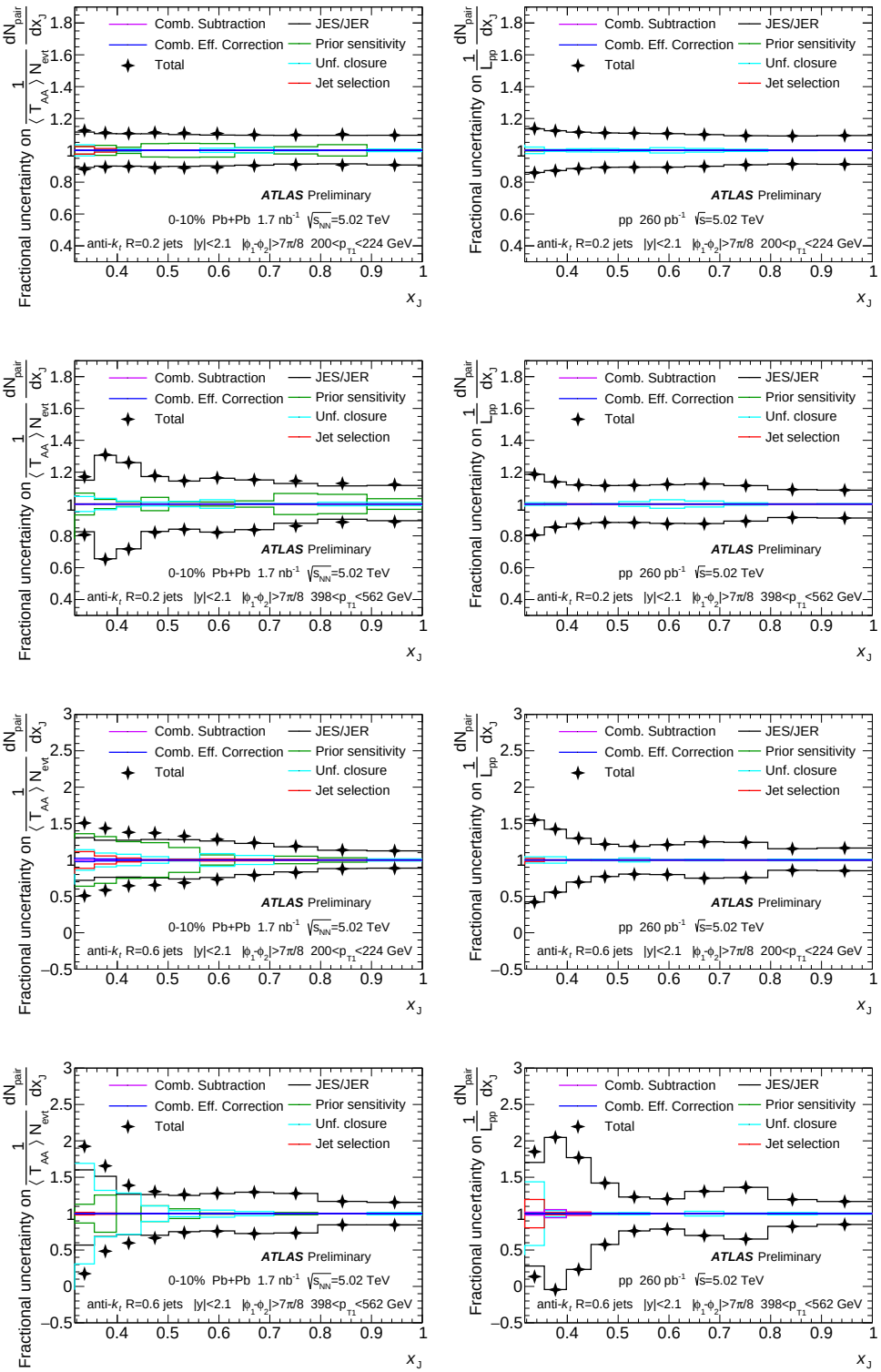

Figure 2: The systematic uncertainty components for the absolutely normalized x_J distributions in 0–10% central Pb+Pb collisions (left) and pp collisions (right) for $R = 0.2$ (top two rows) and $R = 0.6$ (bottom two rows) jets for leading jets with $200 < p_{T,1} < 224$ GeV (left) and $398 < p_{T,1} < 562$ GeV (right).

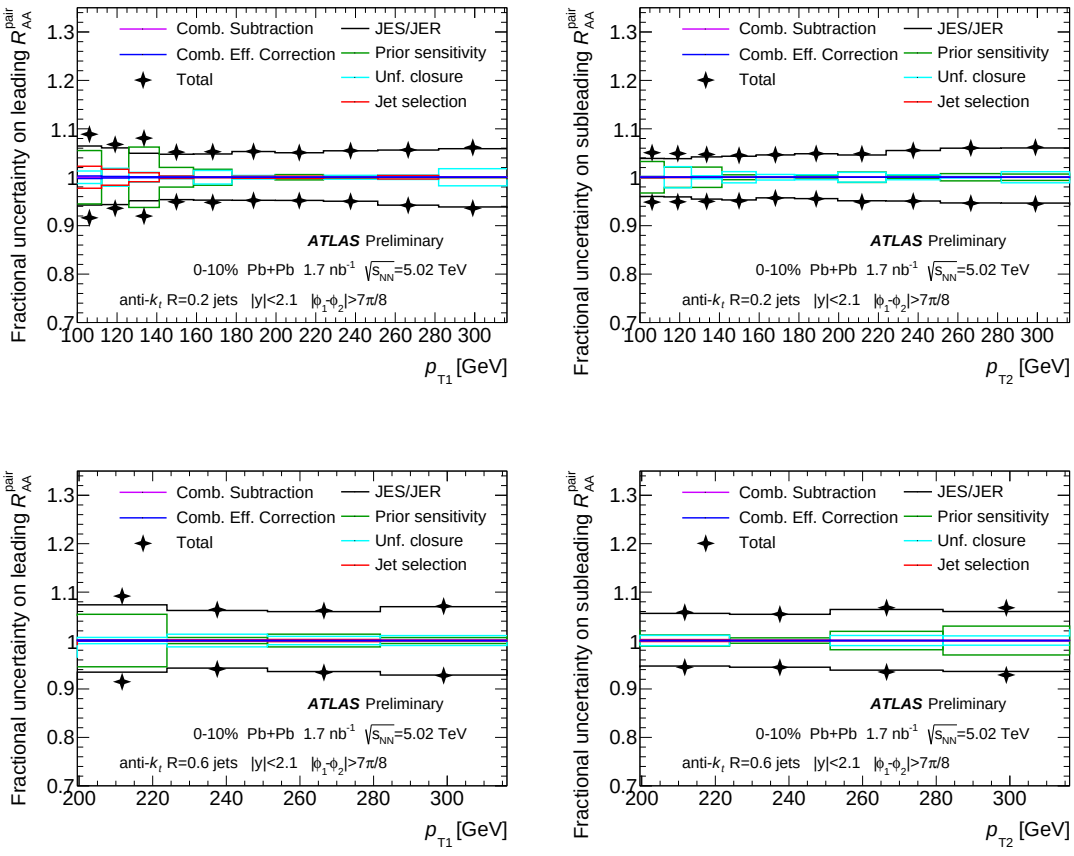

Figure 3: The systematic uncertainty breakdown of the $R_{\mathrm{AA}}^{\mathrm{pair}}$ for leading (left) and subleading (right) $R = 0.2$ (top) and $R = 0.6$ (bottom) jets. The uncertainties on the T_{AA} and pp luminosity values are not shown.

7 Results

7.1 Absolutely Normalized x_J distributions

The absolutely normalized x_J distributions, as defined in Eq (4), are shown in Fig. 4 for pp collisions for leading jets with $200 < p_{T,1} < 224$ GeV and $398 < p_{T,1} < 562$ GeV for all jet radii considered here. The shape of the distributions are very similar for the two $p_{T,1}$ selections shown. In both cases, the distributions are peaked toward balanced dijets as expected. The distributions are more sharply peaked at $x_J \approx 1$ for larger radius jets. This is expected if the larger radius jets cluster together radiation that would be reconstructed as separate jets for the smaller radii.

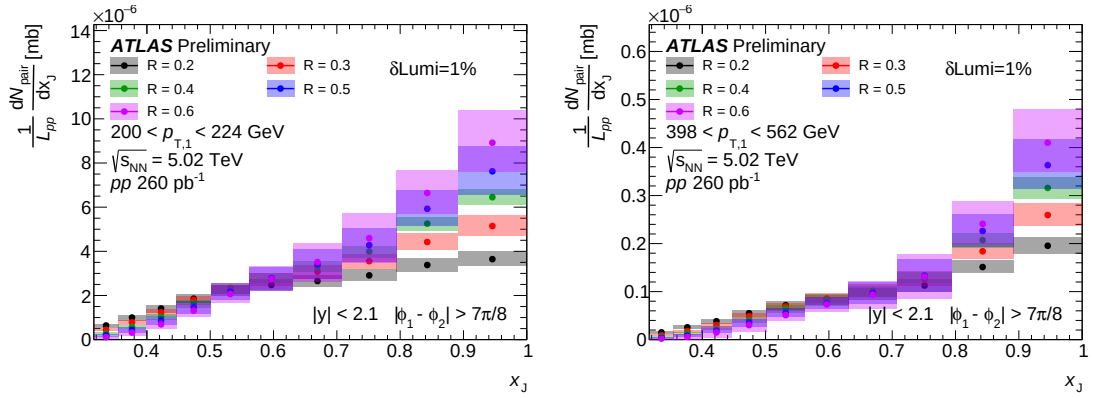

Figure 4: The absolutely normalized x_J distributions in pp collisions (bottom row) for leading jets with $200 < p_{T,1} < 224$ GeV (left) and $398 < p_{T,1} < 562$ GeV (right). Results for $R = 0.4$ jets are from Ref. [19].

Fig. 5 shows the radius dependence of the absolutely normalized x_J distributions in 0–10% and 20–40% central Pb+Pb collisions as defined in Eq. (5) for the same $p_{T,1}$ selections as shown for pp collisions. The x_J distributions in Pb+Pb collisions are broadened compared to those in pp collisions. The magnitude of the modification is larger for lower $p_{T,1}$ values and for the more central collisions. For the $200 < p_{T,1} < 224$ GeV, in mid-central collisions the peak at balanced dijets remains, but becomes weaker as the jet radius decreases; for this $p_{T,1}$ selection in 0–10% central collisions, the distributions are nearly flat for $R = 0.2$, $R = 0.3$, and $R = 0.4$ [19] jets for $x_J > 0.5$. For larger radius jets some peak remains. For the $398 < p_{T,1} < 562$ GeV selection, the x_J distributions in both central and mid-central Pb+Pb collisions remain peaked at $x_J \approx 1$ for the jet radii considered here.

In order to look more closely at the centrality dependent modification from the distributions in pp collisions, Fig. 6 shows the overlaid x_J distributions for 0–10%, 20–40%, and 40–60% central Pb+Pb collisions with those from pp collisions for two $p_{T,1}$ selections, 200–224 GeV and 398–562 GeV for $R = 0.2$, $R = 0.3$, $R = 0.5$, and $R = 0.6$ jets (the $R = 0.4$ results are available in Ref. [19]). As expected, x_J distributions in the most central collisions are the most modified with respect to those in pp collisions for all R values. Additionally, as observed for $R = 0.4$ jets [19], the rate of balanced dijets is strongly suppressed going from pp collisions to central Pb+Pb collisions. For $x_J < 0.6$ values, the rates of dijets become smaller for all R values.

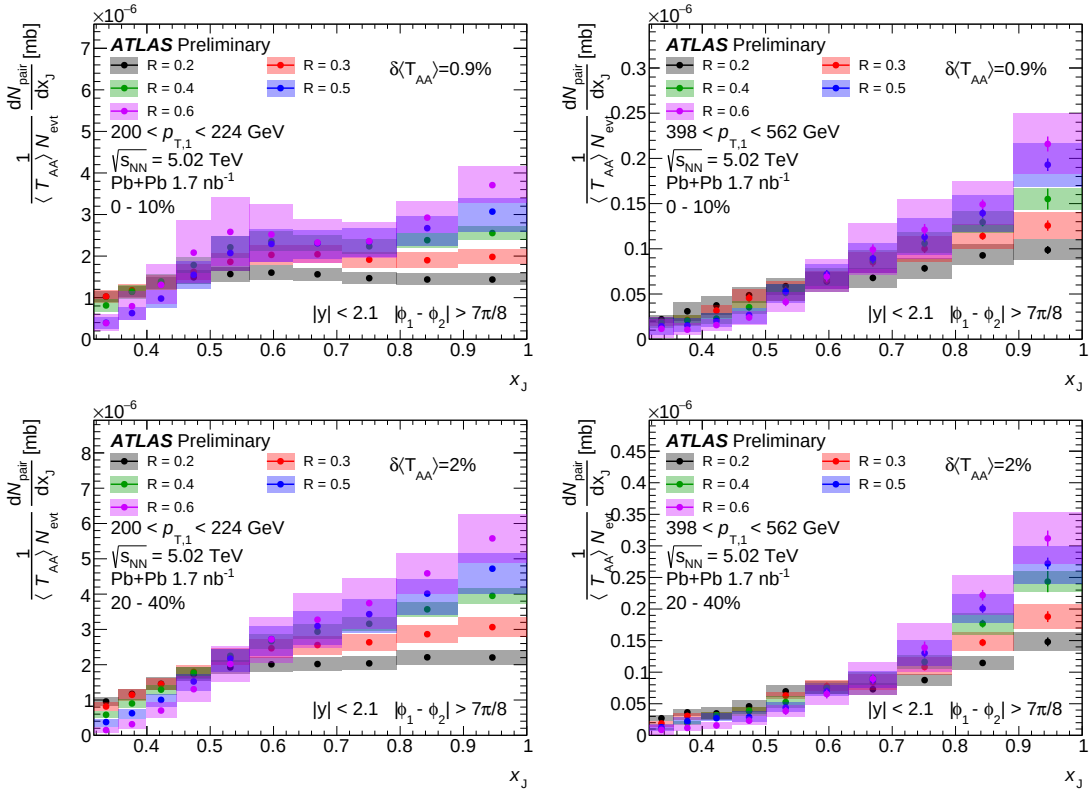

Figure 5: The absolutely normalized x_{J} distributions in 0-10% central Pb+Pb collisions (top row), 20–40% central Pb+Pb collisions (bottom row) for leading jets with $200 < p_{\mathrm{T},1} < 224$ GeV (left) and $398 < p_{\mathrm{T},1} < 562$ GeV (right). Results for $R = 0.4$ jets are from Ref. [19].

7.2 J_{AA} distributions

The J_{AA}, as defined in Eq. (6), allows a direct comparison between the dijet rates in Pb+Pb and pp collisions for specific $p_{\mathrm{T},1}$ and x_{J} selections. First, the J_{AA} distributions for various centralities and $200 < p_{\mathrm{T},1} < 224$ GeV are shown in Fig. 7 for the different jet radii. In 0–10% central collisions, there is a suppression of the number of balanced (high x_{J}) dijets and an enhancement of jets with $x_{\mathrm{J}} < 0.4$. The magnitudes of these effects are approximately constant in R. In 20–40% and 60–80% central collisions the same quantitative trends are observed but the magnitude of the deviations from unity is smaller.

In order to look directly at the jet radius dependence of the dijet momentum balance, the J_{AA} distributions as a function of x_{J} are overlaid for the same $p_{\mathrm{T},1}$ selection (200–224 GeV) for three centrality selections, 0–10%, 20–40%, and 60–80% central Pb+Pb collisions in Fig. 8. The J_{AA} values for $R = 0.4$ jets are calculated from the absolutely normalized x_{J} distributions published in Ref. [19]. At high-x_{J}, the J_{AA} values show no R dependence, despite the significant changes in the x_{J} distributions themselves. At low-x_{J}, there is a spread of the central values of J_{AA} as a function of R and the uncertainties are larger. In order to more directly evaluate the radial dependence of these distributions, the J_{AA} is plotted as a function of the jet radius, for several $p_{\mathrm{T},1}$ selections at selected x_{J} values in the most central collisions in Fig. 9. For nearly balanced dijets ($0.89 < x_{\mathrm{J}} < 1.0$), no significant R dependence to J_{AA} is observed for any $p_{\mathrm{T},1}$ selections. However, as the dijets become more imbalanced, J_{AA} increases with increasing jet radius. This is especially true for lower $p_{\mathrm{T},1}$ selections. One possible explanation is that the subleading jets which have

lost energy, and thus become imbalanced, recover some of the lost energy as the jet radius increases.

7.3 $R_{\mathrm{AA}}^{\mathrm{pair}}$ distributions

The values of $R_{\mathrm{AA}}^{\mathrm{pair}}$ are shown for $R = 0.2$ and $R = 0.6$ jet radii in Fig. 10. For both jet radii, the $R_{\mathrm{AA}}^{\mathrm{pair}}(p_{\mathrm{T},1})$ is larger than $R_{\mathrm{AA}}^{\mathrm{pair}}(p_{\mathrm{T},2})$ for all p_{T} considered here. For the $R = 0.2$ jets both $R_{\mathrm{AA}}^{\mathrm{pair}}(p_{\mathrm{T},1})$ and $R_{\mathrm{AA}}^{\mathrm{pair}}(p_{\mathrm{T},2})$ increase with increasing p_{T}; for $R = 0.6$ jets there is not a strong p_{T} dependence over the measured range. In order to more directly evaluate the radial dependence of these distributions, the $R_{\mathrm{AA}}^{\mathrm{pair}}$ is shown as a function of the jet radius, for two $p_{\mathrm{T},1}$ selections, 200–224 GeV and 282–316 GeV, in 0–10% central collisions in Fig. 11. No radius dependence is observed for either $p_{\mathrm{T},1}$ selection.

The double ratio $R_{\mathrm{AA}}^{\mathrm{pair}}(p_{\mathrm{T},1})/R_{\mathrm{AA}}^{\mathrm{pair}}(p_{\mathrm{T},2})$ of the subleading jet with respect to the leading jet is shown in Fig. 12 for dijets with $200 < p_{\mathrm{T},1} < 316$ GeV as a function of both jet radius and centrality. The overall trend as a function of centrality is as expected for all jet radii; the most central collisions show the most jet suppression and the most peripheral collisions show the least jet suppression. The jet radius dependence of this ratio is isolated for both central and peripheral collisions; no significant jet radius dependence is observed for either 0–10% or 60–80% central Pb+Pb collisions. For central Pb+Pb collisions the value of this ratio is approximately 0.8. For peripheral collisions, the value is higher, approximately 0.9, but still significantly smaller than unity.

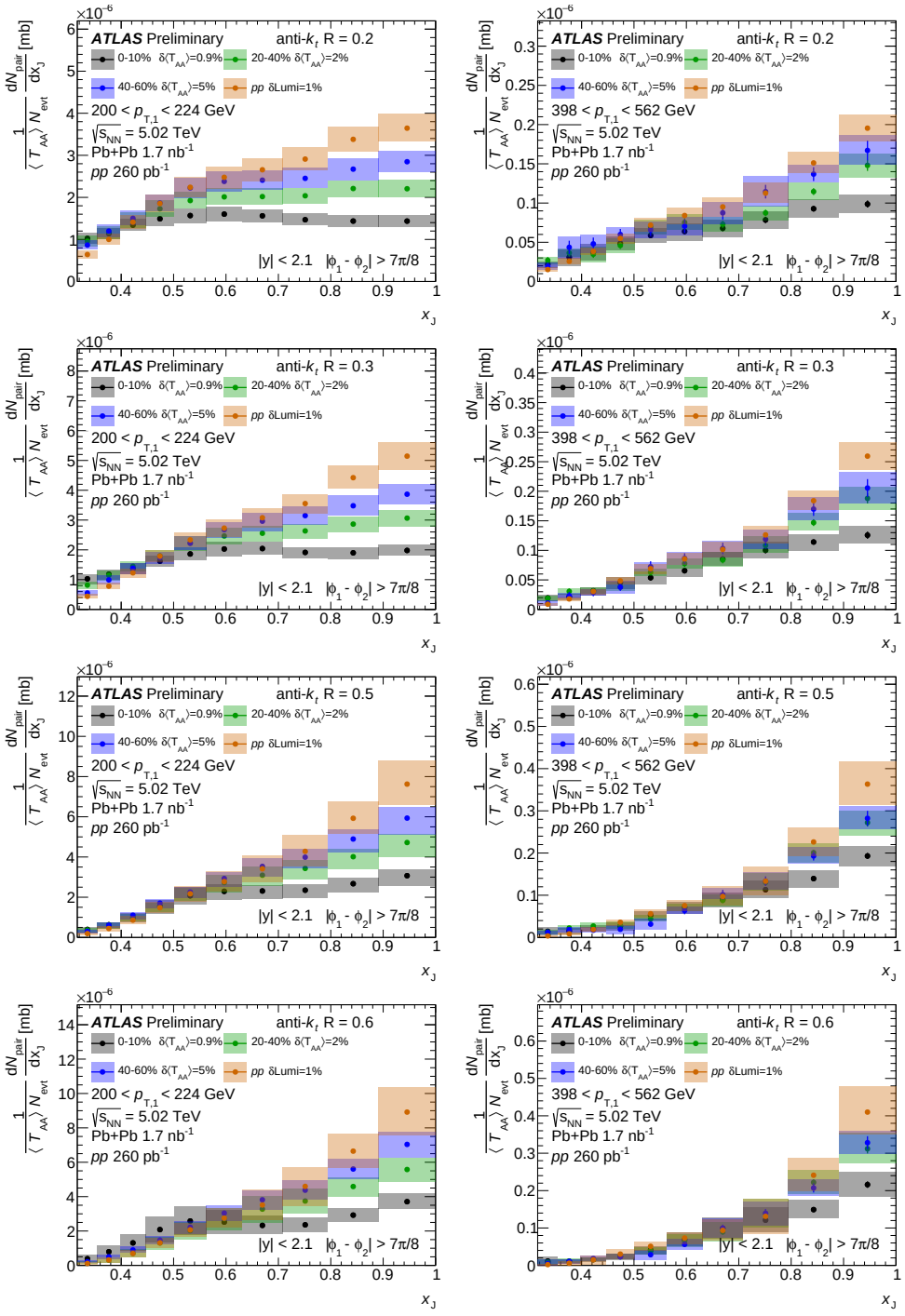

Figure 6: The absolutely normalized x_J distributions for (from top to bottom) $R = 0.2$, $R = 0.3$, $R = 0.5$, and $R = 0.6$ jets for three centrality selections in Pb+Pb collisions and pp collisions. Leading jets with $200 < p_{T,1} < 224$ GeV (left) and $398 < p_{T,1} < 562$ GeV (right) are shown.

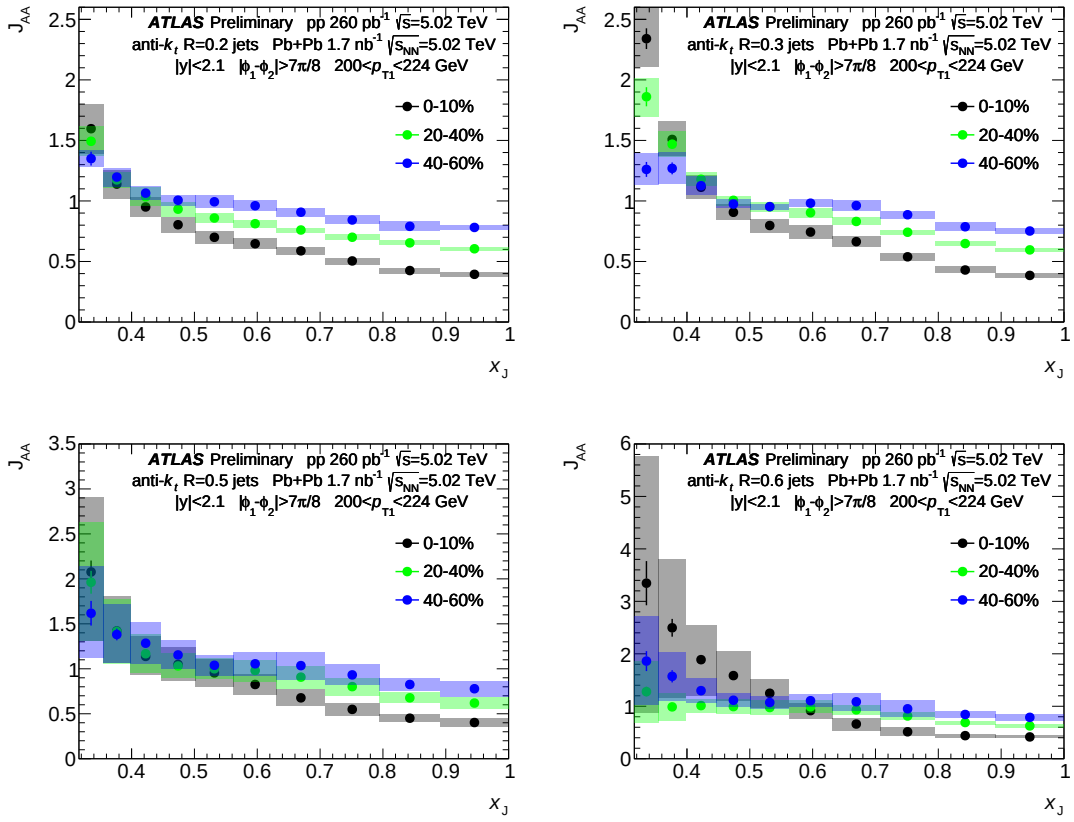

Figure 7: J_{AA} distributions for $R = 0.2$ (top left), $R = 0.3$ (top right), $R = 0.5$ (bottom left), and $R = 0.6$ (bottom right) jets for three centrality selections in Pb+Pb collisions and pp collisions. Leading jets with $200 < p_{\mathrm{T},1} < 224$ GeV are shown. The normalization uncertainties are not shown and are 1.3%, 2.2% and 5.1% for 0–10%, 20–40%, and 40–60% central collisions, respectively.

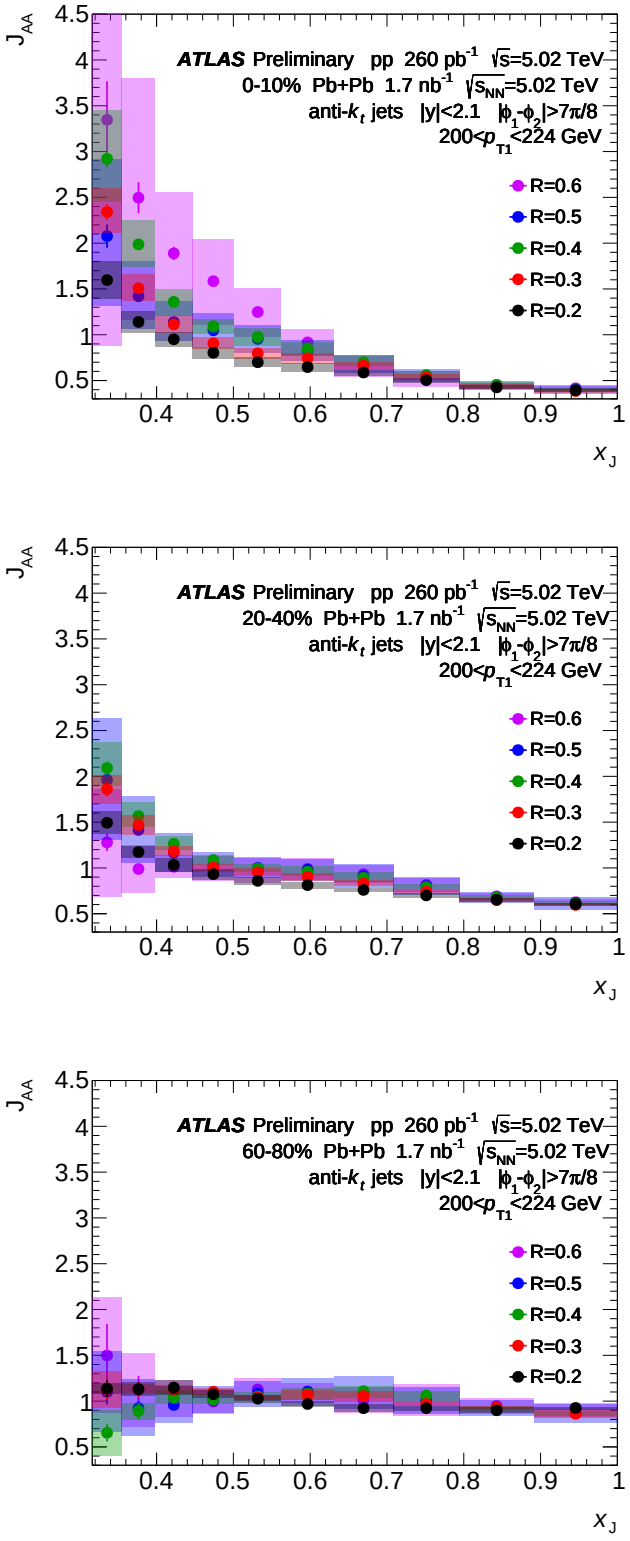

Figure 8: J_{AA} distributions in 0-10% central Pb+Pb collisions (top), 20–40% central Pb+Pb collisions (middle) and 60–80% Pb+Pb collisions (bottom) for leading jets with $200 < p_{\mathrm{T,1}} < 224$ GeV. The normalization uncertainties (not shown) are 1.3%, 2.2% and 8.0% for 0–10%, 20–40%, and 60–80% central collisions, respectively. Results for $R = 0.4$ jets are calculated from Ref. [19].

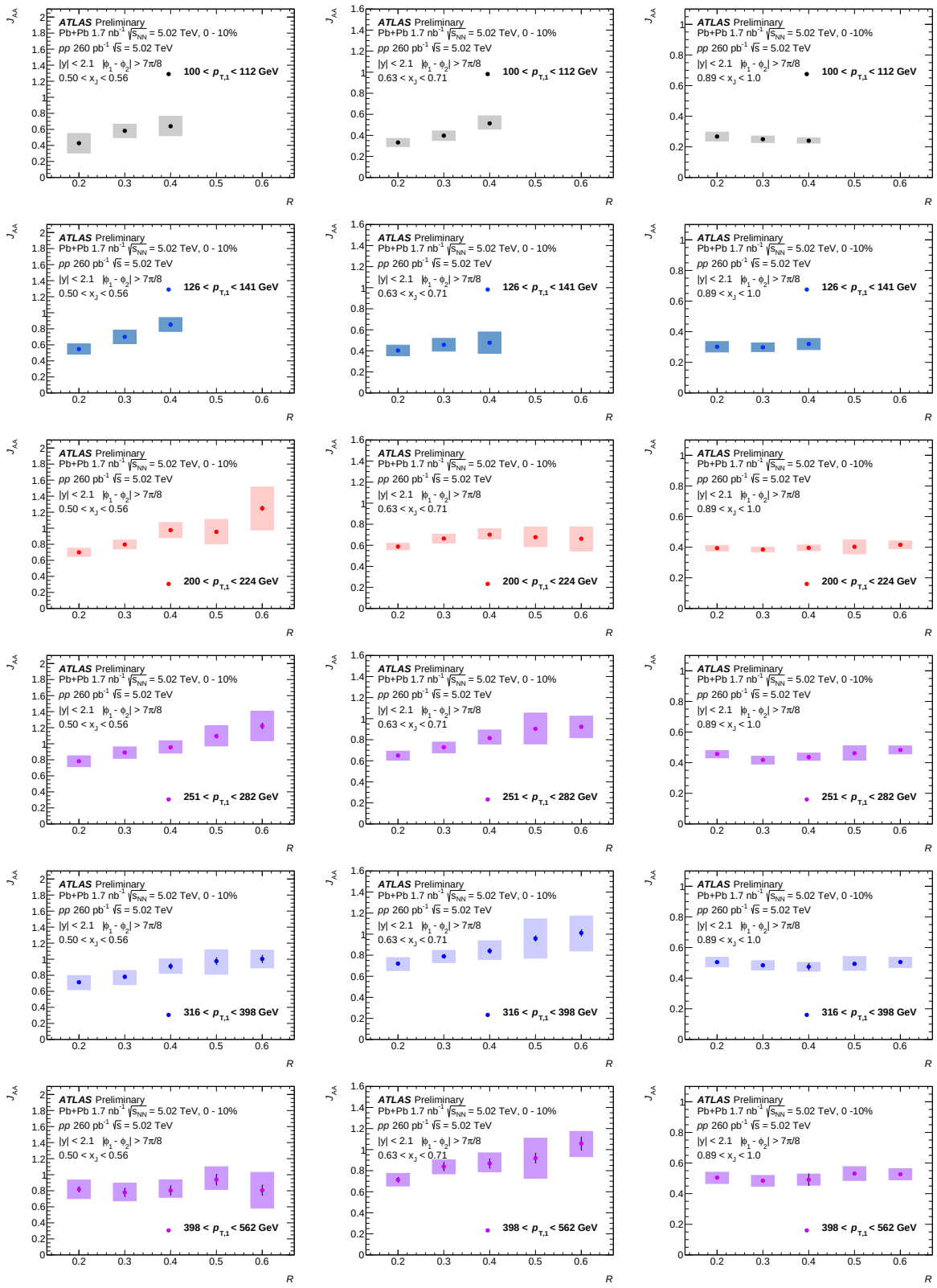

Figure 9: The J_{AA} values as a function of R for jets with (from the top row) $100 < p_{\mathrm{T},1} < 112$ GeV, $126 < p_{\mathrm{T},1} < 141$ GeV, $200 < p_{\mathrm{T},1} < 224$ GeV, $251 < p_{\mathrm{T},1} < 282$ GeV, $316 < p_{\mathrm{T},1} < 398$ GeV, and $398 < p_{\mathrm{T},1} < 224$ GeV in 0–10% central Pb+Pb collisions, for $0.50 < x_{\mathrm{J}} < 0.56$ (left column) $0.63 < x_{\mathrm{J}} < 0.71$ (middle column) and $0.90 < x_{\mathrm{J}} < 1.0$ (right column). There is a 1.3% overall normalization uncertainty common to all points which is not shown. Results for $R = 0.4$ jets are calculated from Ref. [19].

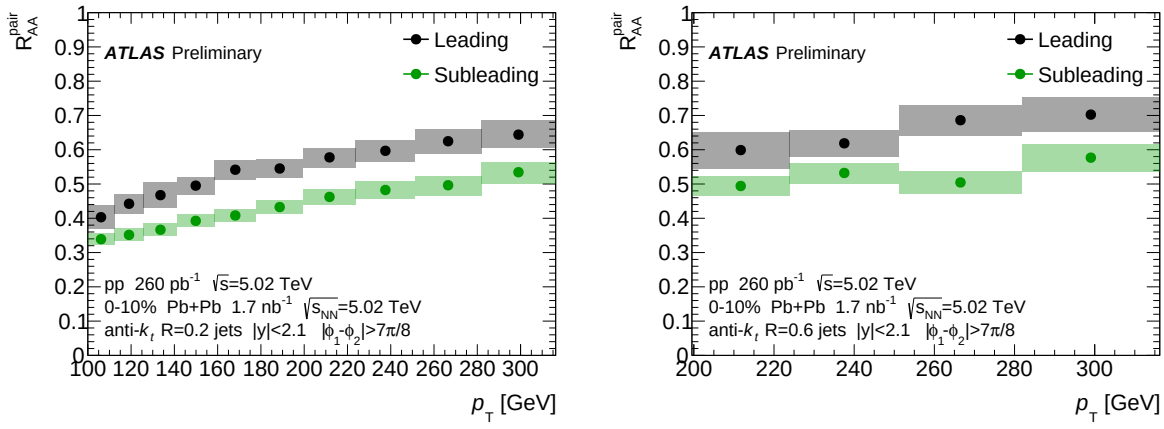

Figure 10: Leading and subleading jet $R_{\mathrm{AA}}^{\mathrm{pair}}$ values as a function of p_{T} for $R = 0.2$ (left) and $R = 0.6$ (right) jets in 0–10% Pb+Pb collisions. There is a 1.3% overall normalization uncertainty common to all points which is not shown.

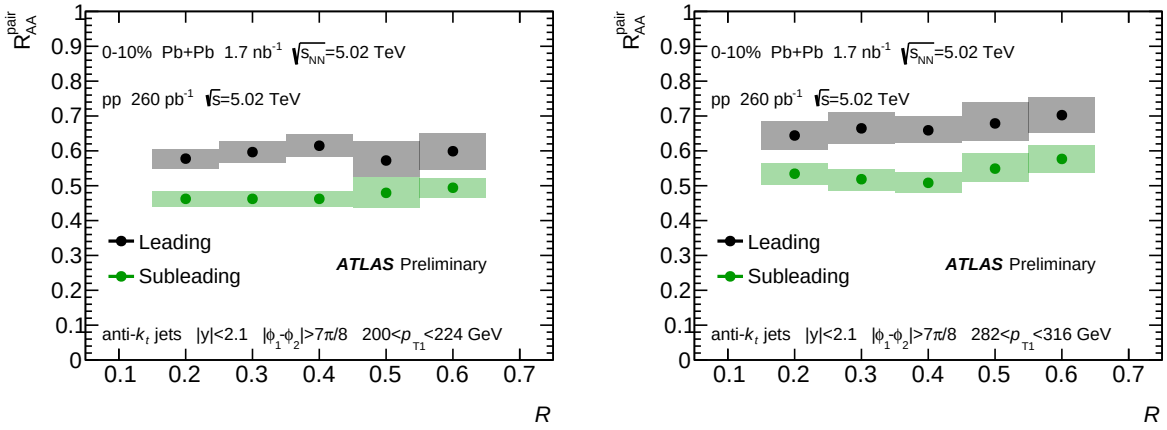

Figure 11: Leading and subleading jet $R_{\mathrm{AA}}^{\mathrm{pair}}$ distributions as a function of jet radius in 0–10% central Pb+Pb collisions, for $200 < p_{\mathrm{T},1} < 224$ GeV (left) and $282 < p_{\mathrm{T},1} < 316$ GeV (right). There is a 1.3% overall normalization uncertainty common to all points which is not shown.

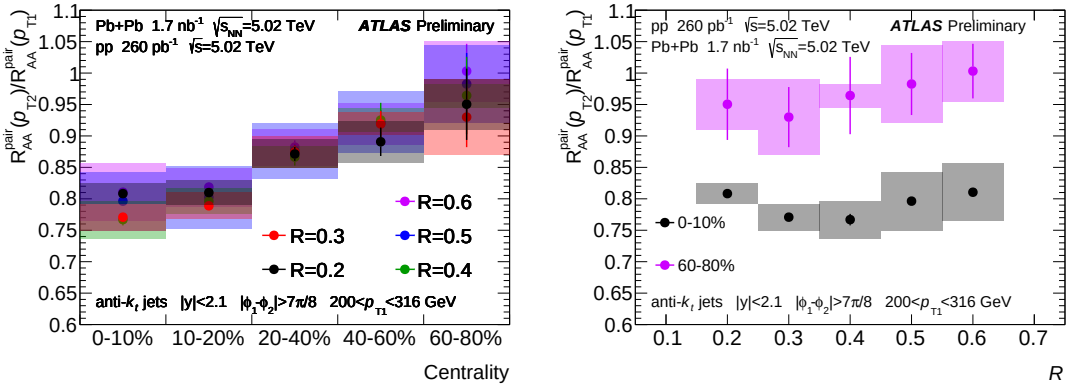

Figure 12: Double ratio $R_{\mathrm{AA}}^{\mathrm{pair}}(p_{\mathrm{T},1})/R_{\mathrm{AA}}^{\mathrm{pair}}(p_{\mathrm{T},2})$ of the subleading and leading jet $R_{\mathrm{AA}}^{\mathrm{pair}}$ distributions as a function of centrality (left), and jet radius (right) for 0–10% and 60–80% central Pb+Pb collisions, for $200 < p_{\mathrm{T},1} < 316$ GeV.

8 Conclusion

This note presents a measurement of the dependence of the dijet momentum balance on jet radius in Pb+Pb and pp collisions at $\sqrt{s_{\mathrm{NN}}}$ = 5.02 TeV. Dijets were studied for jet radii R = 0.2, 0.3, 0.5, and 0.6 by measuring the absolutely normalized x_{J} distributions, as well as the J_{AA} and $R_{\mathrm{AA}}^{\mathrm{pair}}$ ratios, for leading jet p_{T} ranging from 100 GeV to 562 GeV. The results show that larger jet radii give x_{J} distributions peaked towards higher x_{J} values, compared to the smaller jet radii. This is true in both Pb+Pb and pp collisions, but the Pb+Pb collisions show broader and more quenched distributions with respect to pp. The J_{AA} results are constant as a function of R for balanced jets. For imbalanced jets, primarily at low leading jet transverse momentum, the suppression decreases (J_{AA} increases) with increasing R. The $R_{\mathrm{AA}}^{\mathrm{pair}}$ results show that subleading jets are more quenched with respect to leading jets for all the jet radii considered. However, the $R_{\mathrm{AA}}^{\mathrm{pair}}$ does not have a significant dependence on the jet radius in the considered p_{T} range. These results present a comprehensive look at the modification of dijet rates in Pb+Pb collisions compared to pp collisions. These high precision results are complementary to existing results on the jet radius dependence of jet suppression, and will provide important new constraints to theoretical models of jet energy loss.

References

[1] W. Busza, K. Rajagopal and W. van der Schee,
Heavy Ion Collisions: The Big Picture, and the Big Questions,
Ann. Rev. Nucl. Part. Sci. **68** (2018) 339, arXiv: 1802.04801 [hep-ph] (cit. on p. 2).

[2] L. Cunqueiro and A. M. Sickles, *Studying the QGP with Jets at the LHC and RHIC*,
Prog. Part. Nucl. Phys. **124** (2022) 103940, arXiv: 2110.14490 [nucl-ex] (cit. on p. 2).

[3] I. Vitev, S. Wicks and B.-W. Zhang,
A Theory of jet shapes and cross sections: From hadrons to nuclei, JHEP **11** (2008) 093,
arXiv: 0810.2807 [hep-ph] (cit. on p. 2).

[4] M. L. Miller, K. Reygers, S. J. Sanders and P. Steinberg,
Glauber modeling in high energy nuclear collisions, Ann. Rev. Nucl. Part. Sci. **57** (2007) 205,
arXiv: nucl-ex/0701025 (cit. on pp. 2, 5).

[5] ATLAS Collaboration, *Measurement of the nuclear modification factor for inclusive jets in Pb+Pb collisions at* $\sqrt{s_{\mathrm{NN}}} = 5.02$ *TeV with the ATLAS detector*, Phys. Lett. B **790** (2019) 108,
arXiv: 1805.05635 [nucl-ex] (cit. on pp. 2, 3, 6).

[6] CMS Collaboration,
First measurement of large area jet transverse momentum spectra in heavy-ion collisions,
JHEP **05** (2021) 284, arXiv: 2102.13080 [hep-ex] (cit. on p. 2).

[7] ALICE Collaboration,
Measurements of inclusive jet spectra in pp and central Pb-Pb collisions at $\sqrt{s_{\mathrm{NN}}} = 5.02$ *TeV*,
Phys. Rev. C **101** (2020) 034911, arXiv: 1909.09718 [nucl-ex] (cit. on p. 2).

[8] ATLAS Collaboration, *Measurement of suppression of large-radius jets and its dependence on substructure in Pb+Pb collisions at* $\sqrt{s_{\mathrm{NN}}} = 5.02$ *TeV with the ATLAS detector*, (2023),
arXiv: 2301.05606 [nucl-ex] (cit. on p. 2).

[9] D. Pablos, *Jet Suppression From a Small to Intermediate to Large Radius*,
Phys. Rev. Lett. **124** (2020) 052301, arXiv: 1907.12301 [hep-ph] (cit. on p. 2).

[10] CMS Collaboration,
First measurement of large area jet transverse momentum spectra in heavy-ion collisions,
JHEP **05** (2021) 284, arXiv: 2102.13080 [hep-ex] (cit. on p. 2).

[11] ATLAS Collaboration, *Measurement of the jet radius and transverse momentum dependence of inclusive jet suppression in lead-lead collisions at* $\sqrt{s_{NN}}$*= 2.76 TeV with the ATLAS detector*,
Phys. Lett. B **719** (2013) 220, arXiv: 1208.1967 [hep-ex] (cit. on p. 2).

[12] ALICE Collaboration, *Measurement of the radius dependence of charged-particle jet suppression in Pb-Pb collisions at* $\sqrt{s_{NN}} = 5.02$ *TeV*, (2023), arXiv: 2303.00592 [nucl-ex] (cit. on p. 2).

[13] CMS Collaboration, *In-medium modification of dijets in PbPb collisions at* $\sqrt{s_{\mathrm{NN}}} = 5.02$ *TeV*,
JHEP **05** (2021) 116, arXiv: 2101.04720 [hep-ex] (cit. on p. 2).

[14] S. Cao and X.-N. Wang,
Jet quenching and medium response in high-energy heavy-ion collisions: a review,
Rept. Prog. Phys. **84** (2021) 024301, arXiv: 2002.04028 [hep-ph] (cit. on p. 2).

[15] G.-Y. Qin and B. Müller,
Explanation of Dijet Asymmetry in Pb+Pb Collisions at the Large Hadron Collider,
Phys. Rev. Lett. **106** (2011) 162302, arXiv: 1012.5280 [hep-ph] (cit. on p. 2),
Erratum: Phys. Rev. Lett. **106** (2011) 162302.

[16] ATLAS Collaboration, *Measurements of azimuthal anisotropies of jet production in Pb+Pb collisions at* $\sqrt{s_{NN}} = 5.02$ *TeV with the ATLAS detector*, Phys. Rev. C **105** (2021) 064903, arXiv: 2111.06606 [nucl-ex] (cit. on pp. 2, 6).

[17] J. G. Milhano and K. C. Zapp, *Origins of the di-jet asymmetry in heavy ion collisions*, Eur. Phys. J. C **76** (2016) 288, arXiv: 1512.08107 [hep-ph] (cit. on p. 2).

[18] ATLAS Collaboration, *Measurement of jet* p_{T} *correlations in Pb+Pb and* pp *collisions at* $\sqrt{s_{\mathrm{NN}}} = 2.76$ *TeV with the ATLAS detector*, Phys. Lett. B **774** (2017) 379, arXiv: 1706.09363 [hep-ex] (cit. on pp. 3, 8–10).

[19] ATLAS Collaboration,
Measurements of the suppression and correlations of dijets in Pb+Pb collisions at $\sqrt{s_{NN}} = 5.02$ *TeV*, (2022), arXiv: 2205.00682 [nucl-ex] (cit. on pp. 3, 4, 7, 9, 10, 14, 15, 19, 20).

[20] ATLAS Collaboration, *Observation of a Centrality-Dependent Dijet Asymmetry in Lead-Lead Collisions at* $\sqrt{s_{NN}} = 2.77$ *TeV with the ATLAS Detector at the LHC*,
Phys. Rev. Lett. **105** (2010) 252303, arXiv: 1011.6182 [hep-ex] (cit. on p. 3).

[21] CMS Collaboration, *Observation and studies of jet quenching in PbPb collisions at nucleon-nucleon center-of-mass energy = 2.76 TeV*, Phys. Rev. C **84** (2011) 024906, arXiv: 1102.1957 [nucl-ex] (cit. on p. 3).

[22] ATLAS Collaboration, *The ATLAS Experiment at the CERN Large Hadron Collider*, JINST **3** (2008) S08003 (cit. on pp. 3, 4).

[23] M. Cacciari, G. P. Salam and G. Soyez, *The anti-*k_t *jet clustering algorithm*, JHEP **04** (2008) 063, arXiv: 0802.1189 [hep-ph] (cit. on pp. 3, 6).

[24] ATLAS Collaboration,
Luminosity determination in pp *collisions at* $\sqrt{s} = 13$ *TeV using the ATLAS detector at the LHC*, ATLAS-CONF-2019-021, 2019, URL: https://cds.cern.ch/record/2677054 (cit. on p. 4).

[25] ATLAS Collaboration, *ATLAS Insertable B-Layer Technical Design Report*,
ATLAS-TDR-19; CERN-LHCC-2010-013, 2010,
URL: https://cds.cern.ch/record/1291633 (cit. on p. 4),
Addendum: ATLAS-TDR-19-ADD-1; CERN-LHCC-2012-009, 2012, URL:
https://cds.cern.ch/record/1451888.

[26] B. Abbott et al., *Production and integration of the ATLAS Insertable B-Layer*, JINST **13** (2018) T05008, arXiv: 1803.00844 [physics.ins-det] (cit. on p. 4).

[27] ATLAS Collaboration, *Performance of the ATLAS trigger system in 2015*, Eur. Phys. J. C **77** (2017) 317, arXiv: 1611.09661 [hep-ex] (cit. on p. 5).

[28] ATLAS Collaboration, *The ATLAS Collaboration Software and Firmware*, ATL-SOFT-PUB-2021-001, 2021, URL: https://cds.cern.ch/record/2767187 (cit. on p. 5).

[29] ATLAS Collaboration, *Operation of the ATLAS trigger system in Run 2*, JINST **15** (2020) P10004, arXiv: 2007.12539 [physics.ins-det] (cit. on p. 5).

[30] ATLAS Collaboration, *Measurement of longitudinal flow decorrelations in Pb+Pb collisions at* $\sqrt{s_{NN}} = 2.76$ *and 5.02 TeV with the ATLAS detector*, Eur. Phys. J. C **78** (2018) 142, arXiv: 1709.02301 [nucl-ex] (cit. on p. 5).

[31] C. Loizides, J. Kamin and D. d'Enterria, *Improved Monte Carlo Glauber predictions at present and future nuclear colliders*, Phys. Rev. C **97** (2018) 054910, arXiv: 1710.07098 [nucl-ex] (cit. on p. 5), Erratum: Phys. Rev. C **99** (2018) 019901.

[32] ATLAS Collaboration, *Measurement of* $W^{\pm}$ *boson production in Pb+Pb collisions at* $\sqrt{s_{\mathrm{NN}}} = 5.02$ *TeV with the ATLAS detector*, Eur. Phys. J. C **79** (2019) 935, arXiv: 1907.10414 [nucl-ex] (cit. on p. 5).

[33] T. Sjöstrand et al., *An introduction to PYTHIA 8.2*, Comput. Phys. Commun. **191** (2015) 159, arXiv: 1410.3012 [hep-ph] (cit. on p. 5).

[34] ATLAS Collaboration, *ATLAS Pythia 8 tunes to 7 TeV data*, ATL-PHYS-PUB-2014-021, 2014, URL: https://cds.cern.ch/record/1966419 (cit. on p. 5).

[35] R. D. Ball et al., *Parton distributions with LHC data*, Nucl. Phys. B **867** (2013) 244, arXiv: 1207.1303 [hep-ph] (cit. on p. 5).

[36] ATLAS Collaboration, *The Pythia 8 A3 tune description of ATLAS minimum bias and inelastic measurements incorporating the Donnachie–Landshoff diffractive model*, ATL-PHYS-PUB-2016-017, 2016, URL: https://cds.cern.ch/record/2206965 (cit. on p. 5).

[37] S. Agostinelli et al., *GEANT4–a simulation toolkit*, Nucl. Instrum. Meth. A **506** (2003) 250 (cit. on p. 6).

[38] ATLAS Collaboration, *The ATLAS Simulation Infrastructure*, Eur. Phys. J. C **70** (2010) 823, arXiv: 1005.4568 [physics.ins-det] (cit. on p. 6).

[39] M. Bähr et al., *Herwig++ physics and manual*, Eur. Phys. J. C **58** (2008) 639, arXiv: 0803.0883 [hep-ph] (cit. on p. 6).

[40] S. Gieseke, C. Röhr and A. Siódmok, *Colour reconnections in Herwig++*, Eur. Phys. J. C **72** (2012) 2225, arXiv: 1206.0041 [hep-ph] (cit. on p. 6).

[41] J. Pumplin et al., *New generation of Parton Distributions with Uncertainties from Global QCD Analysis*, JHEP **07** (2002) 012, arXiv: hep-ph/0201195 (cit. on p. 6).

[42] M. Cacciari, G. P. Salam and G. Soyez, *FastJet User Manual*, Eur. Phys. J. C **72** (2012) 1896, arXiv: 1111.6097 [hep-ph] (cit. on p. 6).

[43] ATLAS Collaboration, *Measurement of the azimuthal anisotropy of charged particles produced in* $\sqrt{s_{NN}} = 5.02$ *TeV Pb+Pb collisions with the ATLAS detector*, Eur. Phys. J. C **78** (2018) 997, arXiv: 1808.03951 [hep-ex] (cit. on p. 6).

[44] ATLAS Collaboration, *Jet energy measurement and its systematic uncertainty in proton-proton collisions at* $\sqrt{s} = 7$ *TeV with the ATLAS detector*, Eur. Phys. J. C **75** (2015) 17, arXiv: 1406.0076 [hep-ex] (cit. on p. 6).

[45] ATLAS Collaboration, *Jet energy scale and its uncertainty for jets reconstructed using the ATLAS heavy ion jet algorithm*, ATLAS-CONF-2015-016, 2015, URL: https://cds.cern.ch/record/2008677 (cit. on pp. 6, 9).

[46] ATLAS Collaboration, *Measurement of photon-jet transverse momentum correlations in* 5.02 *TeV Pb+Pb and pp collisions with ATLAS*, Phys. Lett. B **789** (2019) 167, arXiv: 1809.07280 [hep-ex] (cit. on p. 6).

[47] G. D'Agostini, *A Multidimensional unfolding method based on Bayes' theorem*, Nucl. Instrum. Meth. A **362** (1995) 487 (cit. on p. 8).

[48] T. Adye, *Unfolding algorithms and tests using RooUnfold*, 2011, arXiv: 1105.1160 [physics.data-an] (cit. on p. 8).

[49] ATLAS Collaboration, *Measurements of the suppression and correlations of dijets in Xe+Xe collisions at* $\sqrt{s_{NN}} = 5.44$ *TeV*, (2023), arXiv: 2302.03967 [nucl-ex] (cit. on p. 9).

[50] ATLAS Collaboration, *Jet energy scale measurements and their systematic uncertainties in proton-proton collisions at* $\sqrt{s} = 13$ *TeV with the ATLAS detector*, Phys. Rev. D **96** (2017) 072002, arXiv: 1703.09665 [hep-ex] (cit. on p. 9).

[51] ATLAS Collaboration, *Measurement of jet fragmentation in Pb+Pb and pp collisions at* $\sqrt{s_{NN}} = 5.02$ *TeV with the ATLAS detector*, Phys. Rev. C **98** (2018) 024908, arXiv: 1805.05424 [nucl-ex] (cit. on pp. 9, 10).

[52] ATLAS Collaboration, *Jet energy scale and resolution measured in proton–proton collisions at* $\sqrt{s} = 13$ *TeV with the ATLAS detector*, Eur. Phys. J. C **81** (2021) 689, arXiv: 2007.02645 [hep-ex] (cit. on p. 10).